Development of a SPECT-Based Three-Dimensional Treatment Planning System for Radioimmunotherapy

Huan B. Giap, Daniel J. Macey and Donald A. Podoloff

Departments of Radiation Physics and Nuclear Medicine, The University of Texas M.D. Anderson Cancer Center, Houston, Texas

Two major obstacles in the development of improved methods for more accurate dose estimates for radioimmunotherapy have been the difficulty in obtaining an accurate patient-specific three-dimensional activity map in vivo and calculating the resulting absorbed dose. We propose a method for three-dimensional internal dosimetry that integrates the three-dimensional activity map from SPECT with a dose-point kernel convolution technique to provide the three-dimensional distribution of absorbed dose. **Methods:** Accurate activity quantitation was achieved with appropriate methods. The count density map from SPECT images was converted into an activity concentration map with a calibration phantom approach. This map was then convolved with an ^{131}I dose-point kernel and three-dimensional fast Fourier transform to yield three-dimensional distribution of absorbed dose, which was then processed to provide the absorbed dose distribution in regions of interest. **Results:** The accuracy of quantitative SPECT was validated to be within 16%. The calculated penetrating radiation absorbed dose was verified with thermoluminescent dosimeter measurements to be within 8%. With standard organs and configuration, the method calculated absorbed dose in good agreement with the MIRD formalism (less than 14%). **Conclusion:** This method overcomes the limitations of planar imaging techniques and the current routine implementation of the MIRD formalism. The results can be processed to provide the absorbed dose distribution in regions of interest and parameters for treatment optimization. Absorbed dose distribution from any plane can be graphically displayed in various ways.

Key Words: single-photon emission computed tomography; radioimmunotherapy; three-dimensional internal dosimetry

J Nucl Med 1995; 36:1885–1894

The principle of radioimmunotherapy (RIT) is to use radiolabeled antibodies as carriers of radionuclides for the selective destruction of a tumor. RIT should be particularly beneficial for the treatment of tumors not easily amenable to surgical control and for the treatment of early recurrence and distant metastases (*1*). Over the past decade, there have been more than 100 RIT and radioimmunodiagnosis clinical trials (*2*). A variety of malignancies have been treated including: hepatoma, neuroblastoma, melanoma, breast, kidney, lung, colon, lymphoma and ovarian malignancies. Theoretically, RIT has the potential to deliver radiation more selectively to a tumor than external beam radiation. Even though RIT is still in the developmental stage, results from preliminary RIT clinical trials are promising. The most common radionuclide used in RIT is ^{131}I. Although ^{131}I has been successfully used to treat thyroid cancer and other malignancies for more than four decades, dose estimates for ^{131}I therapies are still uncertain. These dose estimates require calculation of the activity in a specified volume of interest and accurate methods for calculation of the absorbed dose. Accurate determination of absorbed dose for organs and tumors in patients treated with RIT is essential to establish fundamental dose-response relationships for efficacy and toxicity, which cannot be extrapolated from the dose-response data derived for external beam therapy. These estimates are required to guide the therapist in optimizing a treatment planning strategy for each RIT patient (i.e., to specify the minimum administered activity required to elicit significant therapeutic responses and, more importantly, to specify the maximum administered activity that does not exceed normal tissue toxicity limits).

The complicated movement of circulating monoclonal antibodies (MAbs) through and within tumors, which results in nonuniform distribution, can be explained by at least two factors. First, the irregular tumor vasculature produces a complex pattern of diffusion gradients through which the MAb is transported throughout the tumor (*3*). Second, immunohistochemical studies with MAbs have shown that the antigens against which the MAbs have been directed are not usually expressed uniformly in the whole tumor cell population. Several investigators have observed nonuniform distributions for a variety of antibodies and tumor types in animal and human studies (*4–10*). This heterogeneity was observed on both the macroscopic and microscopic levels. Inspection of SPECT transverse-section images with radiolabeled MAb demonstrates consid-

Received Nov. 4, 1994; revision accepted May 15, 1995.
For correspondence or reprints contact: Huan B. Giap, MD, PhD, Department of Radiation Medicine, Loma Linda University Medical Center, 11234 Anderson St., Loma Linda, CA 92354.

erable heterogeneity of activity distribution in organs and tumor at the macroscopic level.

In some clinical trials of radiolabeled MAb, organ activities have been quantified by planar imaging methods and average organ absorbed doses calculated by the MIRD formalism and standard man S factors (*11*). The planar imaging method, however, suffers from several deficiencies. First, because planar images use only two views of a three-dimensional source distribution in the body, activities estimated from such two-dimensional images generally suffer from superposition of two or more source organs. Second, planar images generally cannot provide accurate estimates of depth-dependent three-dimensional distribution of activity within tumors or normal tissues. Accordingly, although it may be acceptable for uniform activity distributions within normal organs, planar activity quantitation is inadequate for the nonuniform activity distributions of MAbs typically found in tumors. Third, the two-dimensional planar images do not generally provide accurate functional volumetric information necessary for calculation of dose distribution. Therapy radionuclides are selected to deliver most of their dose locally by nonpenetrating radiation. Therefore, significant errors in dose estimates can result if the functional volume does not match the anatomic volume defined by CT or MRI images (*12,13*). These three deficiencies of planar imaging methods can potentially be overcome by SPECT.

The MIRD formalism, as currently implemented, is widely accepted for calculation of absorbed dose in RIT and has served as the framework to provide dose estimates. The advantages in the use of MIRD S-factors are ease of application, availability of tabulated data, standardization of dose estimates among different investigators and extensive validation. There are several disadvantages in the use of the MIRD S-factors, however, including: (a) assumption of uniform distribution of activity in each source organ, (b) assumption of uniform deposition of radiation energy in target regions, (c) lack of information about the distribution of absorbed dose in selected organs of interest, (d) use of fixed idealized anatomic models (i.e., standard man, child or woman) for organ sizes and shapes and (e) lack of S-factors for tumor volumes.

Because no S-factors are available for target volumes other than those defined in the MIRD approach for the standard man, dose estimates for tumors in particular have been a challenge (*14*). An improved method is required for dose estimations when the underlying assumptions made by MIRD S-factors are not applicable. With planar imaging methods and MIRD S-factors, the errors of normal organ dose estimates may be as much as 200%, and most of this inaccuracy comes from the uncertainties in the assessment of the distribution of radioactivity in both tumors and organs (*15*). This may account in part for the large range of dose responses reported in recent RIT trials.

This paper proposes a method for internal dosimetry of ^{131}I based on SPECT. Accurate SPECT quantitation was achieved with appropriate methods for noise filtering, attenuation correction, and correction for Compton scatter and septal penetration. The count density maps from SPECT images were converted to activity concentration maps with a calibration phantom approach. The activity concentration maps were convolved with an ^{131}I dose-point kernel and a three-dimensional fast-Fourier transform approach to yield three-dimensional distribution of absorbed dose. The three-dimensional absorbed dose map was then processed to provide the absorbed dose distribution in regions of interest (ROIs). This method can overcome the limitation of planar imaging methods and MIRD S-factors (i.e., it can provide heterogeneous distributions of absorbed dose in source volumes of any size (down to the limitation set by spatial resolution of SPECT) and shape with nonuniform distributions of activity).

A three-dimensional dosimetry program can provide the unique information required to compare different radionuclide therapy protocols, e.g., to match the emission of a radionuclide (type of particles and energy) with the required dose distribution. In addition, the three-dimensional information on absorbed dose may be more valuable in the interpretation of the responses of heterogeneous antibody and dose distributions and would supplement information from the analysis of clinical response with dose-volume histograms or isodose distribution. A three-dimensional map of the activity distribution is desirable in clinical applications to demonstrate qualitatively and quantitatively the temporal and spatial distribution of the radionuclide in tumors and organs.

MATERIALS AND METHODS

An overview of the proposed three-dimensional treatment planning method is outlined in Figure 1, which includes two major components: activity quantitation by SPECT and absorbed dose calculation. The principal components of quantitative SPECT are noise filtering, subtraction of Compton scatter, boundary detection, image reconstruction, correction for attenuation and conversion of count density into activity concentration. The three-dimensional activity distributions are then converted to absorbed dose with a dose-point kernel convolution technique. The program was written in FORTRAN and compiled using the Lahey 32-bit compiler (Lahey Computer System, Inc., Incline Village, NV), which contains graphic subroutines for image display. The program was developed on a 486-DX2 (66 MHz) IBM-compatible personal computer with 16 MB RAM. The computer code consists of two modules: SPECTRIT and DOSEFFT. SPECTRIT, which stands for "quantitative SPECT for RIT," performs activity quantitation with projection data acquired from an Anger camera system. DOSEFFT, which stands for "dose calculation by fast Fourier transform (FFT)," provides the absorbed dose from the activity map furnished from SPECTRIT, which prompts the user to select options from menus, that includes methods of noise filtering, scatter correction, image reconstruction and attenuation correction. The user can bypass all these menus with a default method at the beginning of the program. The user can also use a pointing device (mouse) to select target volume and to obtain information such as functional volume, descriptive statistics of activity or dose or activity/dose profile plots about an ROI. DOSEFFT can provide important parameters for treatment opti-

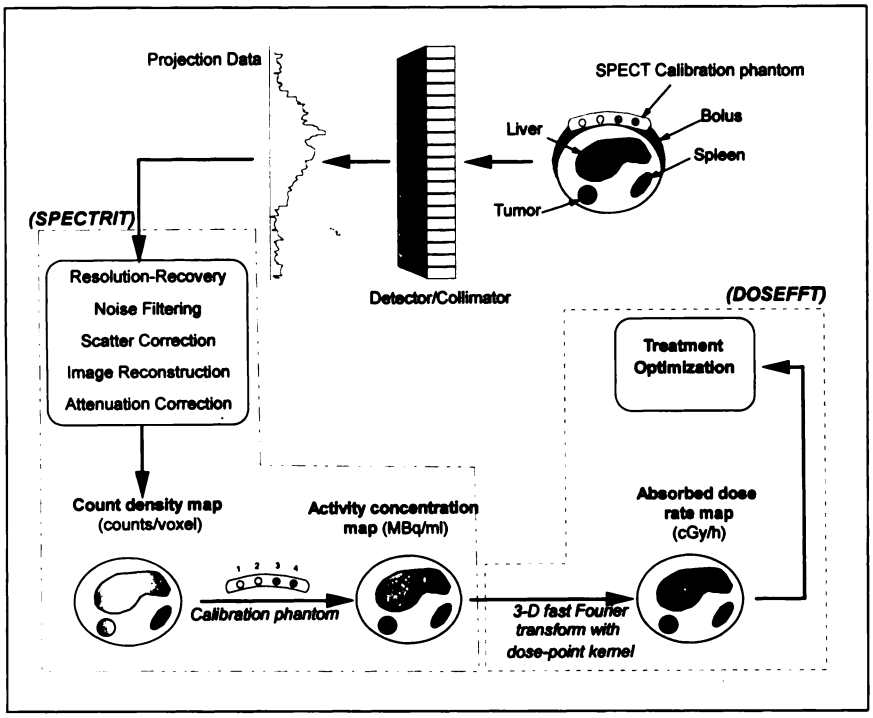

FIGURE 1. Overview of SPECT-based three-dimensional treatment planning strategy for internal dosimetry. Objective is to determine three-dimensional distribution of absorbed dose rate. SPECT method was developed to provide three-dimensional activity distribution, which was then convolved with dose-point kernel technique to provide three-dimensional map of absorbed dose rate. Components of the SPECTRIT and DOSEFFT computer codes are outlined with dashed lines.

mization, such as differential and integral dose-volume histograms, isodose distributions, dose statistics (range, average and s.d.), points of regret and so forth. Absorbed dose distribution from any plane can be graphically displayed as line isodose, gray scale, colorwash, line profile and three-dimensional surface display from transverse, coronal or sagittal views.

The diagram in Figure 1 only shows the calculation of absorbed dose rate from a single SPECT study. To calculate total absorbed dose for a RIT study, the time-dependent SPECT-based activity measurement must be converted to cumulated activity by numeric integration of a fitted time-activity function, which is described in detail in references 11, 16 and 17.

Data Acquisition

SPECT projection data were acquired with a Trionix dual-headed BIAD gamma camera (Trionix Research Laboratory, Inc., Twinsburg, OH). The acquisition parameters were 64 × 64 matrix, 45 projection views for each detector, 20 sec/view, circular orbit with radius of rotation of 27.3 cm and a high-energy parallel-hole collimator. Three energy windows were used to acquire projection data for ^{131}I. The photopeak window of 15% width was centered at 364 keV. The lower scatter window (15% width) was located directly below the photopeak window. The upper scatter window (15% width) was located directly above the photopeak window. The total projection counts acquired were 9.3 million (5 million from the photopeak window and 2.6 million and 1.7 million from the lower and upper scatter windows). The projection data (binary format) were transferred by Ethernet link to the personal computer for all SPECT processing. The section images were reconstructed in a 128 × 128 matrix with 5.3 × 5.3-mm pixel size and 10.6-mm slice thickness.

SPECT Quantitation

Methods for SPECT quantitation include noise filtering, correction for Compton scatter and septal penetration, image reconstruction, boundary detection and attenuation correction. General discussion of SPECT quantitation can be found in Macey and Giap (*18*). For the studies in this paper, the projection data were filtered with a Metz filter, which was optimized specifically for ^{131}I and the Trionix BIAD system (*19*). The Metz filter has been found to improve image quality and activity quantitation significantly compared with conventional low-pass filters (*20–24*). The Metz filter is the default noise filter for SPECTRIT, but the user can select any conventional low-pass filters such as the ramp, Shepp-Logan, Hann, Hamming, Parzen and Butterworth.

The subtraction of Compton scatter and septal penetration was performed before image reconstruction with a modified convolution-subtraction method with a dual-energy window (MCS-DEW) (*25*). This method can be considered a combination of the Jaszczak et al. (*26*) dual-energy window (DEW) approach with constant multiplier and the Axelsson et al. (*27*) convolution subtraction (CS) method. The major disadvantage of DEW is the assumption of a constant scatter fraction in the photopeak window at all projection bins and views. This assumption may be valid for a source located centrally in a symmetric scattering medium (such as a water cylinder) but may be invalid when the source moves off center or when the scattering medium is nonuniform. The CS method provides scatter fractions that are dependent on source locations, but its major disadvantage is the assumption of the spatial symmetry of the scatter distribution (i.e., the left and right wing of the scatter distribution curve are the same and can be described by a monoexponential function). This may explain why it does not predict scatter distributions when the source is off center or near the periphery of a transverse section. The CS method does not utilize any information from the scatter window, which can provide information about the symmetry of the scatter distribution. The MCS-DEW attempts to correct for these deficiencies in both methods. Knowledge of the spatial distribution and magnitude of data collected from a scatter window is used to predict the scatter fraction of photopeak events at each location (projection bins and angles). The method relies on estimates of the scatter fraction in the photopeak projection windows (P_P) from events detected in an overlapping scatter window

(P_S) before reconstruction. An estimate of the true photopeak projection events (P_T) is given by

$$P_T = P_P - c \cdot P_S \otimes Q, \qquad \text{Eq. 1}$$

where $\otimes$ denotes a convolution operation, c is an optimized constant and Q is the scatter transfer function, which convolves with the projection data from a scatter window to yield an estimate of the scatter fraction in the photopeak window. The function Q, which is expressed in terms of spatial frequency, is the ratio of two modulation transfer functions (MTF): one MTF characterizes the scatter data under the photopeak window; the other MTF represents the scatter data in the scatter window (*28*). The user can select other scatter correction methods in SPECTRIT such as convolution subtraction, dual-energy window with constant scatter fraction, DEW with conditional scatter fraction (*29*) or triple-energy window methods (*30*).

The default image reconstruction method for SPECTRIT is the filtered backprojection algorithm, but the user can select other methods from the RECLBL Library [provided by the Lawrence Berkeley Laboratory of The University of California (*31*)] such as the iterative least-squares technique, backprojection of filtered projections and configuration-space convolution algorithm.

Photon attenuation may be the single most significant factor in quantitative SPECT. Attenuation is a more significant problem in SPECT than in PET and other conventional imaging systems (CT and MRI) because the detected photons are at much lower count densities. To correct for attenuation in SPECT, the following parameters are required: (1) an accurate distribution of counts in the object, (2) an accurate boundary of the transverse section and (3) the distribution of attenuating tissues in the object expressed as an attenuation map appropriate for the ECT photon energy. A new postreconstruction attenuation method, called postreconstruction inverse of the sum of geometric means (PRIGM), was used in this study (*32*). The PRIGM method corrects each pixel (i, j) in the reconstructed image for attenuation by multiplication by an average attenuation correction factor C(i, j), defined as

$$C(i,j) = \frac{1}{\frac{2}{N} \cdot \sum_{n=1}^{n=N/2} [e^{\mu \cdot L(i,j,\theta_n)} \cdot e^{\mu \cdot L(i,j,\theta_n + \pi)}]^{1/2}}, \qquad \text{Eq. 2}$$

where N is the total number of projection angles, n is the index for projection angle θ, $L(i, j, \theta_n)$ is the distance from pixel (i, j) to the body outline along the projection view n (or angle θ_n) along which the summation takes place and μ is the effective attenuation coefficient for the photons used for imaging. Note that the attenuation map is used in the calculation of the attenuation correction factor C(i, j), not the emission projection data. This method is similar to the approach introduced by Chang (*33*).

$$C'(i,j) = \frac{1}{\frac{1}{N} \cdot \sum_{n=1}^{n=N} e^{\mu \cdot L(i,j,\theta_n)}}. \qquad \text{Eq. 3}$$

The Chang's correction factor C'(i, j) is the inverse of the arithmetic average of all attenuation path length; PRIGM takes the geometric mean of conjugate attenuation path lengths for the correction matrix. The PRIGM correction matrix is less perturbed near the edges of organs of nonuniform attenuation because the exponential terms are weighted by the conjugate terms. For uniformly attenuating medium, the equation for PRIGM can be simplified to

$$C(i,j) = \frac{1}{\frac{2}{N} \cdot \sum_{n=1}^{n=N/2} e^{\mu/2(L(i,j,\theta_n) + L(i,j,\theta_n + \pi))}}. \qquad \text{Eq. 4}$$

The user can select other methods for attenuation correction in SPECTRIT such as the Chang or iterative least-square intrinsic method.

The object boundary and attenuation map are required for all attenuation correction methods. In SPECT, the term boundary is usually reserved to describe the body or object contours. The difficulty in boundary detection is due to the low spatial resolution, Compton scatter and high noise levels characteristic of SPECT images. The problem becomes more significant as the size of an object decreases and the contrast between the object and background activity decreases. A small error in defining the boundary can lead to significant errors in attenuation correction. The authors used a simple method of boundary detection that uses an adaptive thresholding technique with a gray-level histogram applied to data in a scatter image (*34–36*). Evaluation of the performance of the method with a 22-cm diameter cylinder phantom filled with uniform activity concentrations indicated good boundary definition to ±1 cm. Advantages of this method include no modification to the hardware, no separate transmission scan, simple implementation and quick execution. This method, however, does not provide the attenuation map required for correction of nonuniform attenuating media. This shortcoming can be resolved with a specially designed detector system that could perform simultaneous transmission CT (TCT) and SPECT to provide the map of attenuation coefficients and anatomy of the patient (*37,38*). The new generation of detector systems, such as the Trionix TRIAD and ADAC Genesis VERTEX, offer simultaneous TCT-ECT capability.

SPECT Calibration Method

Most quantitation methods for SPECT depend on a determination of sensitivity from a phantom of the same size and shape as the body section, and the use of the sensitivity measured from this phantom to convert the counts in the section image to activity. Other methods that have been used to convert SPECT counts to activity include calibration of SPECT counts with the conjugate view planar method (*39*), retrospective calibration by activity concentration in urine (*40*) or measurement of the activity concentration in peripheral blood (*41*). Conversion of the counts in a transverse section image to activity requires a sensitivity factor, which should be based on a multitude of acquisition and image processing parameters (*42*). Detector sensitivity can be considered a conversion factor (or calibration factor) to convert the count density (number of counts per voxel) in the reconstructed images to activity concentration at the corresponding location in the object. For SPECT, this conversion factor depends on many variables, such as source-to-collimator distance, activity levels, image acquisition parameters, methods of attenuation correction, scatter correction, noise filtering and image reconstruction algorithm.

In this study, a new method of SPECT calibration was used to convert count density to activity concentration with a calibration phantom to be used with the Alderson abdominal phantom (Fig. 2). The schematic of calibration process is shown in Figure 3. It

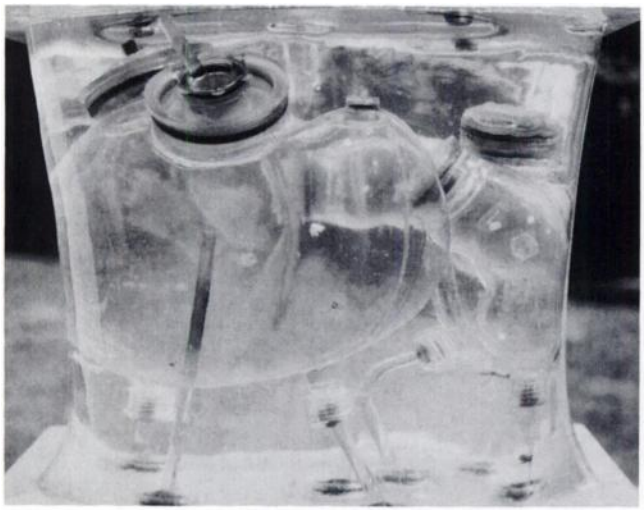

FIGURE 2. Alderson abdominal phantom and SPECT calibration phantom (without bolus).

consisted of four cylindrical tubes that contained measured activity concentrations over a range that covered the anticipated maximum activity concentration in any organ in the body. The tubes, contained in a Lucite housing, were 42 cm long and 1.87 cm in diameter. The tube dimensions were chosen with consideration of the spatial resolution of the detector system, contours of the patient's body and minimal radiation hazard. From the reconstructed images, the count densities and the known activity concentrations of the four tubes were used to construct a calibration curve for every individual section. This calibration curve was a straight line through the four data points fitted by the least-squares technique.

$$A = m_z \cdot C + I_z, \qquad \text{Eq. 5}$$

where A is the activity concentration (in megabecquerels per milliliter), m_z is the slope of calibration curve (in megabecquerels per milliliter per counts per voxel) of transverse section z, C is the count density (in counts/voxel) and I_z is the intercept of the calibration curve (in megabecquerels per milliliter). Count density in any voxel or ROI in the image can be converted to activity concentration with this calibration curve.

Dose-Point Kernel Convolution Technique

The total absorbed dose rate $\dot{D}(r)$ at location r consists of two components: penetrating $[\dot{D}_p(r)]$ and nonpenetrating $[\dot{D}_{np}(r)]$.

$$\dot{D}(r) = \dot{D}_p(r) + \dot{D}_{np}(r). \qquad \text{Eq. 6}$$

The dose rate from nonpenetrating radiations $[\dot{D}_{np}(r)]$ is produced by low-energy gamma, x-ray and beta emissions that deposit all their energy in the SPECT source voxel, which typically has a dimension of 5 mm or greater. The calculation of $\dot{D}_{np}(r)$ is simple because it is equal to the product of the activity concentration A(r, t) and an equilibrium dose constant c_d(c_d = 11.03 cGy-g/MBq-hr or 0.408 cGy-g/hr-μCi for ^{131}I). The dose rate from penetrating radiations $[\dot{D}_p(r)]$ is contributed by high-energy gamma, x-ray and beta emissions, which can deposit energy beyond the source voxel. The calculation of $\dot{D}_p(r)$ is more involved and given by the convolution of activity concentration matrix with a penetrating dose-point kernel (k_p).

$$\dot{D}_p(r) = \int_{V'} A(r') \otimes k_p(r - r') \cdot dV', \qquad \text{Eq. 7}$$

where $\dot{D}_p(r)$ is the absorbed dose rate (in centigrays per hour) from penetrating radiations, A(r') is the activity concentration (in megabecquerels per milliliter) in the voxel at location r' and $k_p(r - r')$ is the penetrating dose-point kernel (in centigrays per megabecquerel per hour) in tissue. The dose-point kernel represents the spherically symmetric dose rate distribution caused by a point source of activity at the center of a sphere. The dose rate at a given distance from a point source of activity in an attenuating and scattering medium has been extensively studied. The dose-point kernel in spheric coordinates can be derived from MIRD Pamphlet No. 2 for photon emissions (*43*) and MIRD Pamphlet No. 7 for beta emissions (*44*). A more fundamental approach is to use a Monte Carlo calculation (*45*) with a computer code such as EGS-4

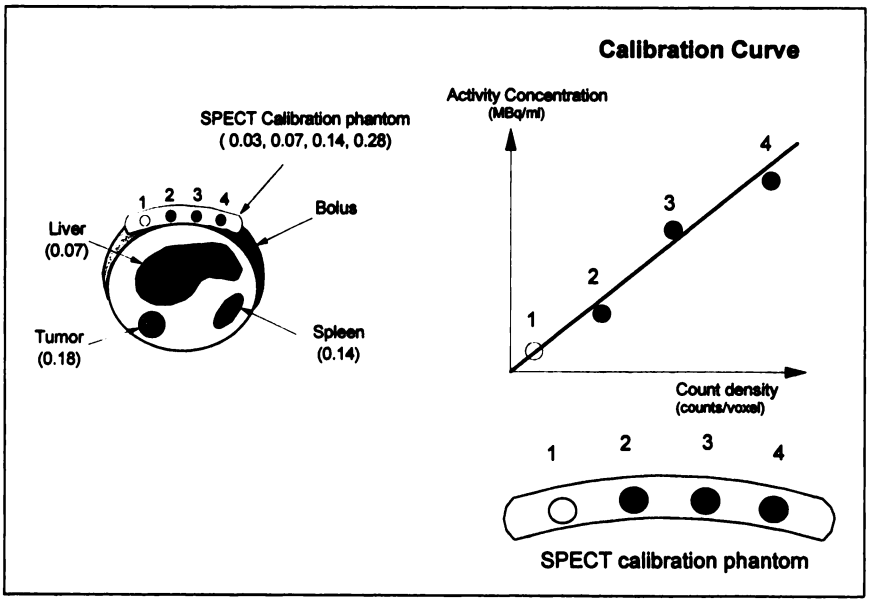

FIGURE 3. SPECT calibration phantom. Activity concentrations of the organs, tumor and calibration phantom are shown in megabecquerels per milliliter. The four tubes of SPECT calibration phantom contain increasing and known activity concentrations. Tubes are contained in Lucite housing. For each reconstructed transverse image, count densities and known activity concentrations of the four tubes are used to construct a calibration curve, which is a straight line fitted through the four data points. Count density at any voxel or ROI in the image can be converted into activity concentration with the calibration curve.

(*46,47*) and ETRAN (*48*). Preliminary studies have shown that the EGS-4 code and MIRD equations provide similar dose-point kernels. In this study, dose-point kernels were calculated by both EGS-4 code and MIRD pamphlets, and this redundancy was used for verification. The dose-point kernel in spherical coordinates was converted into rectangular coordinates to use the three-dimensional FFT operation. This three-dimensional rectangular matrix had to be the same size as the activity matrix, which was 128 × 128 × 32 in this study. The conversion of a spheric, kernel into a rectangular kernel was done with an interpolation algorithm.

The convolution was carried out with a Fourier convolution technique. The procedure applied a three-dimensional fast Fourier transformation of the activity distribution, $F_3\{A(r)\}$, and of the penetrating dose-point kernel, $F_3\{k_p(r)\}$. The subscript 3 indicates that this is a three-dimensional Fourier transform. The complex three-dimensional arrays were multiplied together, and the product was inverse-Fourier transformed to yield the distribution of absorbed dose rate caused by penetrating radiation. The calculation is described by the following equation.

$$\dot{D}_p(r) = F_3^{-1}[F_3\{A(r)\} \cdot F_3\{k_p(r)\}]. \quad \text{Eq. 8}$$

Both penetrating and nonpenetrating components can be calculated by the Fourier convolution method by substitution of the penetrating dose-point kernel k_p by the total dose-point kernel k_{total} in the convolution operation, as follows.

$$\dot{D}(r) = F_3^{-1}[F_3\{A(r)\} \cdot F_3\{k_{total}(r)\}], \quad \text{Eq. 9}$$

where k_{total} is defined as

$$k_{total} = k_p + k_{np}. \quad \text{Eq. 10}$$

Penetrating and nonpenetrating components were calculated separately in this study to examine the magnitude of contributions from the two types of radiation to the total absorbed dose. In clinical applications, in which the total dose is of interest, the k_{total} is used. There is no difference in computer time whether k_{total} or k_p is used in the convolution calculation. Similarly, for a radionuclide that emits only beta particle, such as ^{90}Y, the k_p in the convolution operation includes the contribution from the high-energy beta radiation. The location of the beta particle has to be assumed either at the center of the voxel or distributed uniformly throughout the voxel.

The first phantom, which is shown in Figure 4, was used to validate the dose calculation caused by the penetrating radiations with the three-dimensional FFT approach. This phantom consisted of an 8-cm diameter Lucite rod centered in a 22-cm diameter cylinder filled with ^{131}I at an initial concentration of 0.123 MBq/ml (3.3 μCi/ml) and two thermoluminescent dosimeter (TLD) tubes. Each TLD tube contained 36 small plastic cylinders (5 mm diameter and height) filled with Li_3F powder (TLD-100). The wall thickness of the tissue-equivalent TLD tube was 6 mm, which was sufficient to stop the beta radiation emitted by ^{131}I. The TLD tubes were located in defined positions in an 8-cm diameter Lucite rod that was inserted through the ^{131}I-filled center of the cylinder. The TLDs were exposed to the photons of ^{131}I for one week and then removed from the phantom. After another 2 days, the TLDs were read with a MARK IV TLD reader model 1100 (Radiation Detection Co.). The TLD reading (in voltages per gram of powder) were converted into absorbed dose (in centigrays) with a TLD standard that had been irradiated to a calibrated ^{60}Co beam. The readings were also corrected for nonlinearity. The activity concentration was determined by an assay of the solution

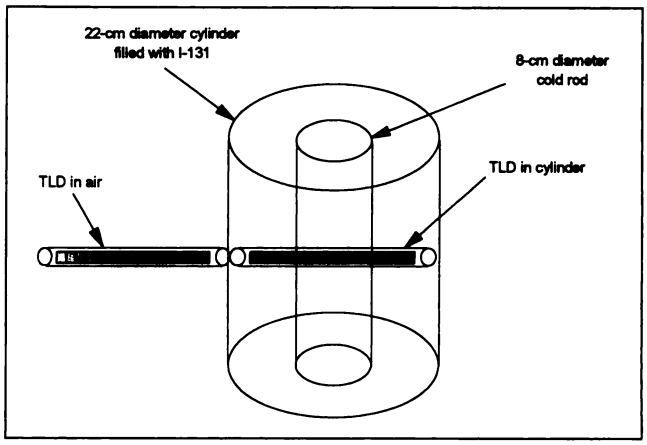

FIGURE 4. Lucite rod (8-cm diameter) centered in the 22-cm diameter cylinder filled with ^{131}I solution. TLD tube contains 36 stacked small TLD capsules.

in the phantom both at the times when the TLDs were inserted and removed. The assay was performed by measurement of the average activity in five aliquots of solution from the phantom with two different detectors (CAPINTEC CRC-7 Capintec, Inc., Ramsey, NJ) and NaI spectrometer model 2600 (Ludlum Instruments, Inc., Sweetwater, TX). SPECT projection images of the phantom were acquired with a Trionix BIAD detector system immediately after the TLDs were removed.

The second phantom used to validate the method was the Alderson abdominal phantom (Fig. 2), which contained various activity concentrations of ^{131}I in the liver, spleen and a spherical tumor (diameter = 5.52 cm). This phantom was scanned with the calibration phantom. The transverse section of these two phantoms is shown in Figure 3. The volumes for the liver, spleen and tumor were 1579, 159 and 88 ml, respectively, and the corresponding activity concentrations were 0.71, 1.4 and 1.8 MBq/ml (1.88, 3.69, 4.94 uCi/ml). The activity concentrations in the calibration tubes were 0.03, 0.07, 0.14 and 0.28 MBq/ml.

RESULTS AND DISCUSSIONS

The TLD measurements of absorbed dose along the diameter of the cylindric phantom are shown in Figure 5, which displays absorbed dose caused by penetrating radiation (D_p) compared with the TLD location. The TLD measurements (circled data points) are compared with the calculated absorbed dose profile shown as a solid line. The results show good agreement (within 8%) between the calculated and measured data inside the phantom (in tissue-equivalent material). Outside the phantom, i.e., in air, the TLD measurement followed the inverse-distance-square pattern, although the calculated dose, which assumed the medium as tissue equivalent, was much higher. This result indicates one limitation of the dose-point kernel convolution technique, which was noted by Meredith et al. (*12*). The dose-point kernel convolution technique is strictly valid only for a homogeneous medium for which the kernels are calculated (in this study, the medium was water). This technique becomes less accurate in regions of the body where different tissue densities coexist, such as lung or bone. Kwok et al. (*49*) reported that the dose to tissue

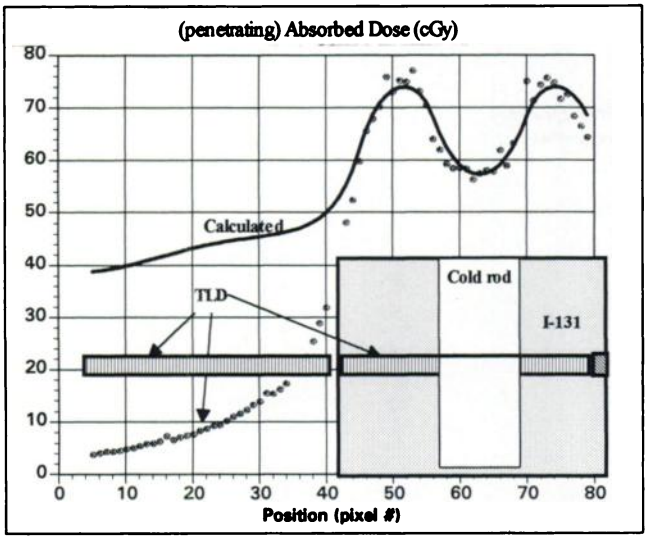

FIGURE 5. Absorbed dose caused by penetrating radiations measured from TLD vs. those calculated by DOSEFFT along the center of ^{131}I-filled 22-cm diameter cylindric phantom with the 8-cm diameter Lucite rod.

within 2 mm of a tissue-bone interface is underestimated by 20% to 40% because of backscatter of low-energy electrons. This limitation is significant for absorbed dose estimates for the thorax and bone marrow.

Three levels of quantitation were evaluated with the Alderson phantom: functional volumes, activity concentrations and absorbed dose rates. The functional volumes are required for activity quantitation and absorbed dose calculation. The approach used for volume quantitation was a gray-level histogram method (GLH) (*50*). For each transverse section, sources from organs and tumor were identified, and edges of organs were found with a threshold selected by the GLH method. The results which showed less than 6% percent difference are shown in Table 1. The good agreement observed here resulted from the following conditions:

1. The phantom sizes and activity concentrations were known in advance.
2. No background activity was present.
3. The tumor did not overlap organs.
4. Tumor volume was larger than the resolution volume of the detector system.
5. Activity concentrations were sufficiently high to provide good SPECT images.

Although these conditions may not be realistic in a clinical setting, the results are nevertheless valid for this experiment. Volumetric calculations from SPECT images are fundamentally challenging because of the limited spatial resolution, Compton scatter and high noise levels characteristic of SPECT images. The problem becomes more significant as the size of an object and the contrast between the object and background activity decrease. Volumetric calculation is a separate problem compared with activity quantitation and dose calculation, and rigorous investigation of this issue is beyond the scope of this present study.

The activity quantitation results were validated by comparison of the true activity concentrations with the values calculated for the whole liver, spleen and tumor. The results are shown in Table 2. The percent differences were 4.4%, −14.3% and −16.3% for the liver, spleen and tumor, respectively. It is well recognized that the accuracy depends on source volume. The error in localization of the edges of larger organs is less. Because the volume of the liver is more than 10 times the volume of either the spleen or tumor, the observed percent difference in activity quantitation for the three organs was as expected. The s.d. indicates the precision of the measurement, which was found to be about 0.3 μCi/ml. The coefficient of variation (COV) is defined as the ratio of the s.d. over the mean and relates to the relative precision of the calculation; the average COV was found to be about 11% for this study. The magnitudes of the s.d. and COV are correlated with the variation of activity concentration within the organs of interest.

The activity distributions of the Alderson abdominal phantom were then used in the calculation of absorbed dose rate by the dose-point kernel convolution technique. The calculated absorbed dose rates were accumulated slice by slice for the whole liver, the spleen and the tumor. These accumulations were used to calculate the average absorbed dose rates for each source volume at the time of the SPECT acquisition. These average absorbed dose rates were then compared with those calculated by MIRD S-factors. The S-factors from MIRD Pamphlet No. 11 (*52*) were corrected for the differences in organ mass in this phantom from those used in the MIRD reference man model. The S-factor for the spheric tumor was derived from MIRD Pamphlet No. 8 (*53*). The results are shown in Table 3. The percentage differences of the mean absorbed dose rate calculated for the two methods were 9.1%, 13.7% and 0.9%

TABLE 1
Accuracy of Volume Determined from SPECT for Source Organs with Iodine-131 in the Alderson Abdominal Phantom

	True volume (ml)	Calculated volume (ml)	Difference (%)
Liver	1579	1620	2.6
Spleen	159	168	5.9
Tumor	88	85	−4.0

TABLE 2
Accuracy of Activity Quantitation from SPECT for Source Organs with Iodine-131 in the Alderson Abdominal Phantom

	True activity concentration (μCi/ml)	Calculated activity concentration (μCi/ml)	Difference (%)	Coefficient of variation (%)
Liver	1.88	1.96	4.4	16
Spleen	3.69	3.16	−14.3	12
Tumor	4.94	4.14	−16.3	6.0

for the liver, spleen and tumor, respectively. MIRD S-factors only provide the mean absorbed dose rate, whereas the convolution technique provides the three-dimensional distribution of dose rate. The results can be processed to provide the absorbed dose distribution in ROIs and parameters for treatment optimization such as differential and integral dose-volume histograms (Fig. 6), isodose distribution, dose statistics (range, average and s.d.), points of regret (cold spot in tumor or hot spot in normal organs) and so forth. Distributions of activity concentration and absorbed dose rate from any plane can be graphically displayed as line isodose, gray-scale, colorwash, line profile and three-dimensional surface display from transverse, coronal or sagittal view (Figs. 7, 8 and 9). Because there are no assumptions with regard to the size, shape and location of target volume, this method can be applied to any patient's anatomy, tumor location and size (limited only by the spatial resolution of the SPECT camera). The three-dimensional FFT calculation for this matrix of 128 × 128 × 16 was completed in 45 sec on a 486-DX2 (66 MHz) personal computer. This high speed was achieved through the efficiency of the FFT algorithm. The reproducibility of the method was evaluated by the repetition of phantom studies with different source configurations and activity concentrations.

CONCLUSION

Accurate specification of radiation absorbed dose is central to all treatment modalities in radiation oncology and to establish fundamental dose-response relationships in RIT. The objective of this study was to develop a method that could provide more accurate RIT dosimetry, which depends on activity quantitation by SPECT and the dose-point kernel convolution technique. The objective of SPECT is to represent the three-dimensional distribution of activity in large tumors and organs accurately within the available spatial resolution. Achievement of this goal is constrained by the physical characteristics of the detector system (variation of spatial resolution and sensitivity across the field of view of the detector), the emission characteristics of radionuclides and the methods used to derive quantitative information from the acquired data (image reconstruction algorithm, noise filter and scatter and attenuation correction methods). Important limitations of this three-dimensional treatment planning approach are di-

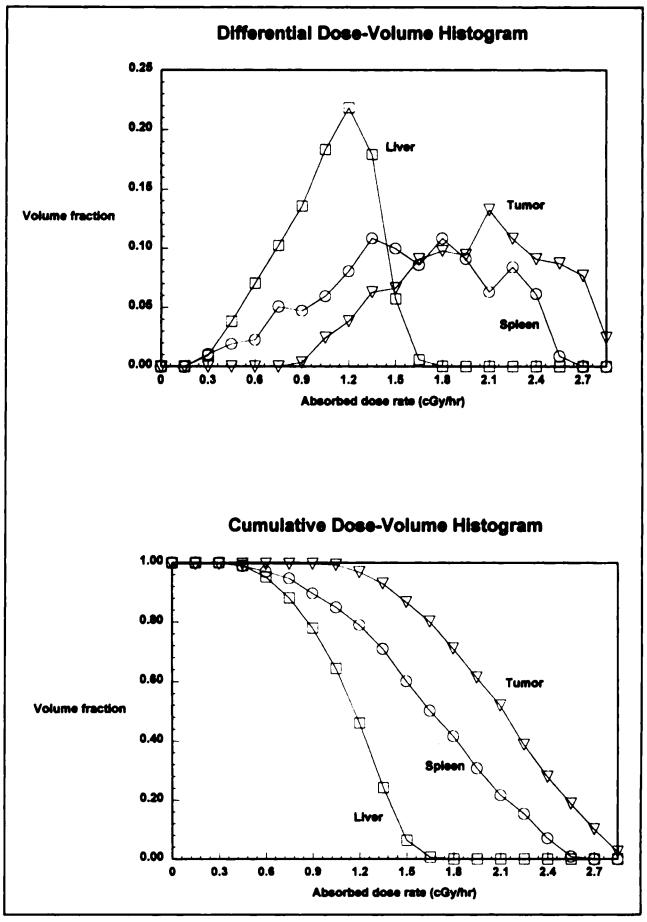

FIGURE 6. Differential and cumulative dose-volume histogram of the spleen, liver and tumor in Alderson abdominal phantom.

TABLE 3
Comparison of Average Absorbed Dose Rate (Both Penetrating and Nonpenetrating Radiation) Calculated for Source Organs in the Alderson Abdominal Phantom

	MIRD average absorbed dose rate (cGy/hr)	Calculated average absorbed dose rate (cGy/hr)	Difference (%)
Liver	1.04	1.14	9.1
Spleen	1.45	1.65	13.7
Tumor	2.08	2.10	0.91

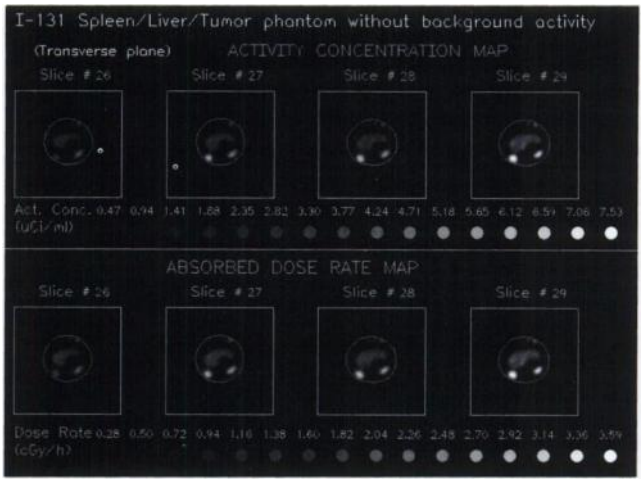

FIGURE 7. Gray-scale images for four transverse sections of the Alderson abdominal phantom. Top row shows activity concentration maps, and bottom row shows absorbed dose rate maps of the corresponding four slices. Locations of liver, spleen, tumor and calibration phantom are similar to the schematic in Figure 3. Gray scales that correlate different shades of gray to the absorbed dose rate and activity concentration are also shown.

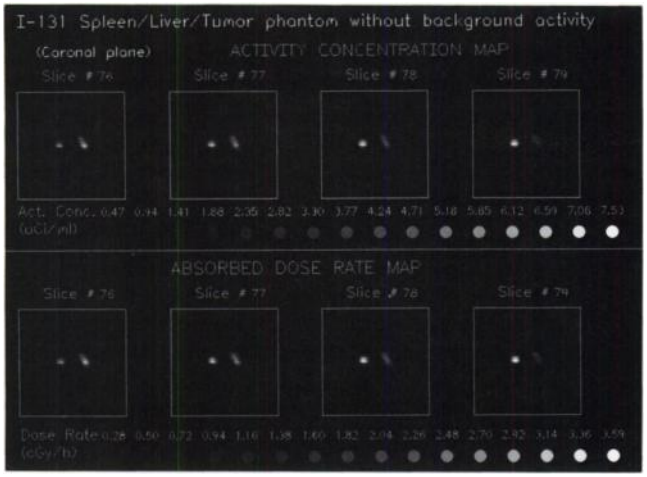

FIGURE 8. Gray-scale images for four coronal sections of Alderson abdominal phantom. Top row shows activity concentration maps, and the bottom row shows absorbed dose rate maps of the corresponding four slices. The round ROI on the left is the tumor, and the oval ROI on the right is the spleen. Gray scales that correlate different shades of gray to the absorbed dose rate and activity concentration are also shown.

rectly related to the inherent limitations of SPECT imaging with an Anger camera. The minimal volume in which absorbed doses can be derived with this method depends on the spatial resolution of the SPECT images, typically 1 to 2 cm. This limits the specification of dose distribution to volumes greater than 8 ml.

Future studies should include the following areas:

1. Investigation of the dose-point kernel convolution technique for heterogeneous tissues, i.e., bone marrow and lung.

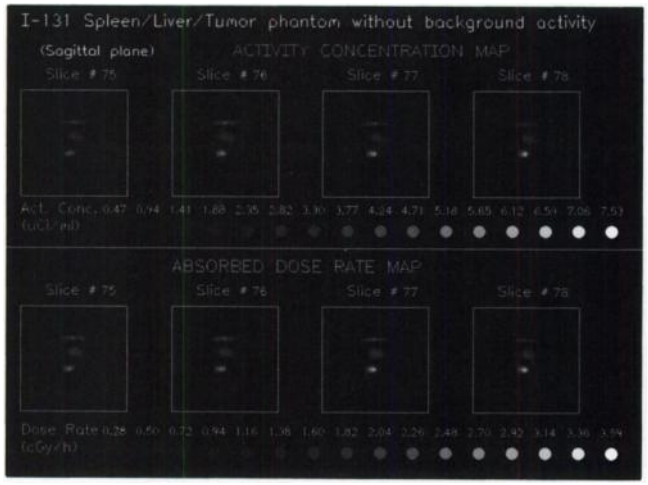

FIGURE 9. Gray-scale images for four sagittal sections of the Alderson abdominal phantom. Top row shows activity concentration maps, and the bottom row shows absorbed dose rate maps of the corresponding four slices. For each image, the top ROI is the calibration tube, the middle ROI is the liver and the bottom ROI is the spleen. Gray scales that correlate different shades of gray to absorbed dose rate and activity concentration are also shown.

2. Dose calculation for bone marrow, which is usually the limiting normal organ for RIT.
3. SPECT quantitation for heterogeneous media, which requires a detector system capable of simultaneous acquisition of transmission and emission images and also methods of image correlation of ECT and TCT images.
4. Validation of the method in RIT patients, which requires a method of measuring absorbed dose in vivo such as implanted miniature-TLDs (*51*).
5. New methods for more accurate volumetric calculations from SPECT images.
6. Extension of the method to other radionuclides.
7. A practical method for calculation of the cumulative activity and total absorbed dose.

ACKNOWLEDGMENTS

This project was funded in part by an MD/PhD fellowship grant of the University of Texas Health Science Center at Houston, the University of Texas M.D. Anderson Cancer Center and National Cancer Institute contract DM91-022. We thank the Lawrence Berkeley Laboratory of the University of California for supplying the RECLBL Library. Dr. Giap thanks Drs. Arthur L. Boyer, Peter Davies, Paul H. Murphy, R. Wanda Rowe and Leonard A. Zwelling.

REFERENCES

1. Mausner LF, Srivastava SC. Selection of radionuclides for radioimmunotherapy. *Med Phys* 1993;20:503–509.
2. Larson SM. Radioimmunology: imaging and therapy. *Cancer* 1991; 67(suppl):1253–1260.
3. Humm JL. Dosimetric aspects of radiolabeled antibodies for tumor therapy. *J Nucl Med* 1986;27:1490–1497.
4. Langmuir VK, Sutherland RM. Radiobiology of radioimmunotherapy: current status. *Antibody Immunoconj Radiopharm* 1988;1:195–211.
5. Jones PL, Gallagher BM, Sands H. Autoradiographic analysis of monoclonal antibody distribution in human colon and breast tumor xenografts. *Cancer Immunol Immunother* 1986;22:139–143.
6. Esteban JM, Schlom J, Mornex F, Colcher D. Radioimmunotherapy of athymic mice bearing human colon carcinomas with monoclonal antibody B72.3: histological and autoradiographic study of effects on tumors and normal organs. *Eur J Cancer* 1987;23:643–655.
7. Griffith MH, Yorke ED, Wessels BW, DeNardo GL, Neacy WP. Direct dose confirmation of quantitative autoradiography with micro-TLD measurements for radioimmunotherapy. *J Nucl Med* 1988;29:1795–1809.
8. Hand PH, Nuti M, Colcher D. Definition of antigenic heterogeneity and modulation among human mammary carcinoma cell populations using monoclonal antibodies to tumor-associated antigens. *Cancer Res* 1983;43: 728–735.
9. Natali PG, Cavaliere R, Bigotti A. Antigenic heterogeneity of surgically removed primary and autologous metastatic human melanoma lesions. *J Immunol* 1983;130:1462–1466.
10. Wright GL, Beckett ML, Starling JJ. Immunohistochemical localization of prostate carcinoma-associated antigens. *Cancer Res* 1983;43:5509–5516.
11. Loevinger R, Budinger TF, Watson EE, eds. *MIRD primer for absorbed dose calculation*. New York: Society of Nuclear Medicine; 1991.
12. Meredith RF, Johnson TK, Plott G, et al. Dosimetry of solid tumors. *Med Phys* 1993;20:583–592.
13. Leichner PK, Klein JL, Garrison JB, et al. Dosimetry of I-131 anti-ferritin in hepatoma, specific activities in the tumor and liver. *Cancer Treat Rep* 1993;67:647–658.
14. Snyder VS, Ford MR, Warner GG. *MIRD pamphlet no. 5. Estimates of specific absorbed fractions for photon sources uniformly distributed in a heterogeneous phantom*. New York: Society of Nuclear Medicine; 1975.
15. Siegel JA, Wessels NW, Watson EE. Bone marrow dosimetry and toxicity for radioimmunotherapy. *Antibotd Immunoconj Radiopharm* 1990;3:213–233.

16. Sorenson JA, Phelps ME. *Physics in nuclear medicine*, 2nd edition. Philadelphia: WB Saunders; 1987.
17. Sharp PF, Dendy PP, Keyes WI. *Radionuclide imaging techniques*. London: Academic Press; 1985.
18. Macey DJ, Giap HB. Quantitative SPECT. In: Kramer EL, Sanger J, eds. *Clinical SPECT imaging*. New York: Raven Press; 1995.
19. Giap HB, Macey DJ, Boyer AL. Development of count-dependent resolution-recovery digital filter for SPECT imaging of iodine-131 [Abstract]. *Med Phys* 1993;20:909.
20. Gilland DR, Tsui BMW, McCartney WH, Perry JR, Berg J. Determination of the optimum filter function for SPECT imaging. *J Nucl Med* 1988;29:643–650.
21. King MA, Doherty PW, Schwinger RB, Jacobs DA, Kidder RE, Miller TR. Fast count-dependent digital filtering of nuclear medicine images: concise communication. *J Nucl Med* 1983;24:1039–1045.
22. King MA, Penney BC, Glick SJ. An image-dependent Metz filter for nuclear medicine imaging. *J Nucl Med* 1988;29:1980–1989.
23. Penney BC, King MA, Glick SJ. Restoration of combined conjugate images in SPECT: comparison of a new Wiener filter and the image-dependent Metz filter. *IEEE Trans Nucl Sci* 1990;37:707–712.
24. King MA, Coleman M, Penney BC, Glick SJ. Activity quantitation in SPECT: a study of pre-reconstruction Metz filtering and use of scatter degradation factor. *Med Phys* 1991;18:184–189.
25. Giap HB, Macey DJ. Evaluation of four scatter correction methods for quantitative SPECT of iodine-131 [Abstract]. *Med Phys* 1993;20:865.
26. Jaszczak RJ, Greer KL, Floyd CE. Improved SPECT quantitation using compensation for scattered photon. *J Nucl Med* 1984;25:893–900.
27. Axelsson B, Msaki P, Israelsson A. Subtraction of Compton-scattered photons in SPECT. *J Nucl Med* 1984;25:290–294.
28. Giap HB, Macey DJ. Scatter correction in SPECT: modified convolution-subtraction with dual-energy window method. *Phys Med Biol* 1995:in press.
29. Macey DJ, Bayouth JE, Boyer AL, Auster M. A new scatter subtraction method for quantitative I-131 SPECT imaging [Abstract]. *Med Phys* 1992; 19:780.
30. Macey DJ, Grant EJ, Bayouth JE, et al. Improved conjugate view quantitation of I-131 by subtraction of scatter and septal penetration events with a triple energy window method. *Med Phys* 1995: in press.
31. Huesman RH, Gullberg GT, Greenberg WL, Budinger TF. *RECLBL library users manual: Donner algorithms for reconstruction tomography*. Berkeley, CA: Lawrence Berkeley Laboratory, University of California; 1977.
32. Giap HB, Macey DJ. Evaluation of three attenuation correction methods for quantitative SPECT [Abstract]. *Med Phys* 1993;20:909.
33. Chang LT. A method for attenuation correction in radionuclide computed tomography. *IEEE Trans Nucl Sci* 1978;25:638–643.
34. Otsu N. A threshold selection method from gray-level histograms. *IEEE Trans Sys Man Cyber* 1979;9:62–66.
35. Mortlemans L, Nuyts J, Van Pamel G, Van den Maegdengerg V, De Roo M, Suetens P. A new thresholding method for volume determination by SPECT. *Eur J Nucl Med* 1986;12:284–290.
36. Giap HB, Macey DJ. SPECT boundary detection using gray-level histogram method and scatter image [Abstract]. *J Nucl Med* 1994;35:196P.
37. Bailey DL, Hutton BF, Walker PJ. Improved SPECT using simultaneous emission and transmission tomography. *J Nucl Med* 1987;28:844–851.
38. Frey EC, Tsui BMW, Perry JR. Simultaneous acquisition of emission and transmission data for improved thallium-201 cardiac SPECT imaging using a technetium-99m transmission source. *J Nucl Med* 1992;33:2238–2245.
39. Macey DJ, Marshall R. The lungs. In: Ell PJ, Holman BL, eds., *Computed emission tomography*. Oxford: Oxford University Press; 1982.
40. Israel O, Iosilevsky G, Front D, et al. SPECT quantitation of I-131 concentration in phantoms and human tumors. *J Nucl Med* 1990;31:1945–1949.
41. Green AJ, Dewhurst SE, Begent RH, Bagshaw KD, Riggs SJ. Accurate quantitation of I-131 distribution in gamma camera imaging. *Eur J Nucl Med* 1990;16:361–365.
42. Jaszczak RJ, Floyd CE, Coleman RE. Scatter compensation techniques for SPECT. *IEEE Trans Nucl Sci* 1984;32:786.
43. Berger MJ. *Energy deposition in water by photons from point isotropic sources. MIRD pamphlet no 2*. New York: Society of Nuclear Medicine; 1978.
44. Berger MJ. *Distribution of absorbed dose around point sources of electrons and beta particles in water and other media. MIRD pamphlet no 7*. New York: Society of Nuclear Medicine; 1978.
45. Dale RG. A Monte Carlo derivation of parameters for use in the tissue dosimetry of medium and low energy nuclides. *Br J Radiol* 1982;55:748–757.
46. Nelson WR, Hirayama H, Rogers DWO. *EGS4 code system. SLAC report 265*. Stanford Linear Accelerator Center, Stanford University; 1985.
47. Rogers DWO, Bielajew AF. Experimental benchmarks of EGS. In: Jenkins TM, Nelson WR, Rindi A, eds., *Monte Carlo transport of electrons and photons*. New York: Plenum; 1988.
48. Berger MJ, Seltzer SM. *ETRAN, Monte Carlo code system for electron and photon transport through extended media*. ORNL documentation RSIC computer code package CCC-107. Oak Ridge, TN: 1973.
49. Kwok CS, Prestwich WV, Wilson BC. Calculation of absorbed doses for nonuniformly distributed beta and gamma radionuclides in soft tissues. *Med Phys* 1985;12:405–412.
50. Mortlemans L, Nuyts J, Van pamel G, Van den Maegdengerg V, De roo M, Suetens P. A new thresholding method for volume determination by SPECT. *Eur J Nucl Med* 1986;12:284–290.
51. Wessels BW, Griffith MM. Miniature thermoluminescent dosimeter absorbed dose measurements in tissue phantom models. *J Nucl Med* 1986;27: 1308–1314.
52. Snyder WS, Ford MR, Warner GG, Watson SB. "S": absorbed dose per unit cumulated activity for selected radionuclides and organs. In: *MIRD pamphlet no. 11*. New York: Society of Nuclear Medicine; 1975.
53. Ellett WH, Humes RM. Absorbed fractions for small volumes containing photon-emitting radioactivity. In: *MIRD pamphlet no. 8*. New York: Society of Nuclear Medicine; 1978.